

Final Technical Report

NEHRP/USGS Award Number: G15AP00106

Periodic Loading, Deformation and Seismicity in California

Prof. Roland Bürgmann
Chris Johnson

Berkeley Seismological Laboratory and
Department of Earth and Planetary Science
University of California, Berkeley
307 McCone Hall
Berkeley, CA 94720-4767

Telephone: 510-643-9545; Fax: 510 643-9980
Email: burgmann@seismo.berkeley.edu

Term covered by this award: 08/01/2015 to 07/31/2016

Abstract

Seasonal crustal stress variations result from hydrospheric loads, pore pressure fluctuations, Earth and ocean tides, and temperature gradients. In California, these processes follow an annual periodic cycle and each contributes to the crustal deformation. First-order models indicate the near surface hydrological mass changes can result in stresses >1 kPa at seismogenic depths, a small stress perturbation that may be associated with rate changes in seismicity. Prior work suggests that areas around the San Andreas Fault (SAF) system exhibit resolvable seasonal periodicity, consistent with forcing by seasonal hydrospheric surface loads and/or subsurface fluid pressures.

To evaluate if statistically significant periodicities in seismicity can be identified in subregions defined by their tectonic setting and deformation style we use the Schuster spectrum, Schuster periodogram, and the multi-frequential periodogram analyses. We examine seismicity in central California, spanning the central SAF system, the Sierra Nevada and the Eastern California shear zone and test the sensitivity of earthquake occurrence with respect to small external stressing due to hydrospheric loading. We explore the effects of choice of minimum event magnitude and magnitude range on the statistical analysis. We also evaluate both original and declustered catalogs, employing a number of different declustering algorithms, to avoid statistical bias due to event clustering associated with interacting earthquakes. Using 26 years of $M \geq 2.5$ catalog data we find statistically significant periods of about 4-, 6-, and 12-months for seismicity located near Parkfield and a 12-month significant period in the Sierra Nevada – ECSZ. Informed by the multi-frequential periodogram analysis and considering possible modulation by loads of known periodicity (e.g., semi-annual and annual tides, seasonal hydrological loads and 14.24-month pole-tide forcing), we evaluate the significance of these apparent periodicities by determining model coefficients of trigonometric functions fit to the seismicity time series.

The apparent modulation of seismicity with a period of one year supports our hypothesis of seasonal loading and warrants modeling the seasonal deformation associated with time varying loads that have near-annual periods. We evaluate the deformation and stress for California faults by considering the contribution of seven periodic loads (atmosphere, Earth pole tides, Earth tides, non-tidal ocean, ocean tides, temperature variations, and water storage). The stress estimates are calculated as forward models at a seismogenic depth of 8 km in California using the fault geometry described in the Uniform California Earthquake Rupture Forecast (UCERF3) fault model to resolve the normal and shear stress components and obtain the Coulomb failure stress. In coastal locations the ocean tides produce large normal-stress changes. In general the largest seasonal stress contribution arises from the seasonal water storage. Depending on fault geometry the addition or removal of water increases the failure stress. Our results suggest a seasonally varying shear and normal stress on the central SAF with a peak-to-peak amplitude of 0.7 and 3.0 kPa, respectively. The largest stress amplitudes are in the normal-stress component on the order of ~ 4 kPa for dipping reverse faults located in the Coast Ranges and along the eastern Sierra Nevada range front. Our results suggest the earthquake populations are modulated at periods of natural loading cycles and failure occurs at times of peak stressing amplitudes. The results provide new insights into the sensitivity of faults to small stress changes and improve our understanding of fault interaction physics.

REPORT

1. Introduction

The distribution of earthquakes in space and time has stochastic and deterministic elements. Earthquakes preferentially occur along and near major, pre-existing faults in plate boundary zones, but some events occur deep within plate interiors. Earthquakes on an individual fault are understood to follow a cycle of long-term tectonic stress accumulation leading to failure at some critical stress level [Reid, 1910]; however, either due to variations in the stressing rate or in the failure stress, the recurrence intervals of earthquakes on a fault tend to vary widely [Chen *et al.*, 2013; Ellsworth *et al.*, 1999].

As earthquakes reflect the release of locally accumulated elastic stress, stress changes from previous earthquakes or non-tectonic loads should influence their timing. For example, the temporal distribution of earthquake populations is strongly influenced by event interactions, evident in the occurrence of foreshocks and aftershocks [Freed, 2005]. In addition to triggering of earthquakes by fault interaction, changes in stress due to other factors, including sub-surface fluid transport and volcanic, glacial, hydrological, and atmospheric loads, may affect the timing of events. A number of these external forces are of cyclical nature, including semidiurnal and longer-period tides, seasonal hydrospheric (i.e., snow, surface- and groundwater) and atmospheric loads and other climate-related cycles, and the ~14-month Chandler wobble of Earth's spin axis. Cyclical stress amplitudes (~0.1-10 kPa) are generally less than the yearly tectonic stress accumulation on plate-boundary fault zones, but appear to suffice to modulate seismicity in some cases.

Much research work has pursued the possibility of tidal earthquake triggering, finding a rather weak correlation of seismicity rates with semi-diurnal tidal stress cycles of the order of a few kPa [e.g., Beeler and Lockner, 2003; Vidale *et al.*, 1998]. Catalogs with very large numbers of events are required to detect a correlation with the short-period tides, possibly because the time scale of earthquake nucleation greatly exceeds that of the periodic forcing [e.g., Beeler and Lockner, 2003]. Tidal modulation is better resolved for cases of particularly strong oceanic tidal loads (normal stress > 10 kPa) in subduction zones [Cochran *et al.*, 2004; Tanaka, 2012]. Non-volcanic tremor sources located below the seismogenic zone in some subduction and strike-slip fault zones appear to be much more susceptible to modulation by the weak, short-period tides than upper-crustal earthquakes [Ide, 2010; Thomas *et al.*, 2012].

Seasonal deformation results from periodic load cycles related to hydrospheric or atmospheric surface loads [Amos *et al.*, 2014; Dong *et al.*, 2002; Gao *et al.*, 2000; Heki, 2003; Namias, 1989], seasonal fluctuations of subsurface pore fluid pressures [Christiansen *et al.*, 2007; Hainzl *et al.*, 2013], and/or seasonal thermoelastic strains induced by atmospheric temperature variations [Ben-Zion and Allam, 2013]. A number of studies find that seismicity correlates with such seasonal forcing [Bettinelli *et al.*, 2008; Bollinger *et al.*, 2007; Gao *et al.*, 2000; Hainzl *et al.*, 2013; Pollitz *et al.*, 2013b]. Bettinelli *et al.* [2008] calculate that crustal stresses associated with surface load changes due to summer monsoon rains in the Ganges Basin amount to ~2-4 kPa in the Himalayan seismic zone, where earthquakes preferentially occur in winter. They suggest that due to the longer period of the seasonal loads, triggering occurs even though the stress changes are not larger than those from the short-period tides, which do not produce a resolvable modulation of seismicity in the region. Gao *et al.* [2000] propose that seasonal atmospheric pressure variations in California exert stress cycles of ~2 kPa and has produced seasonal seismicity in some areas of California for several years after the 1992 Landers

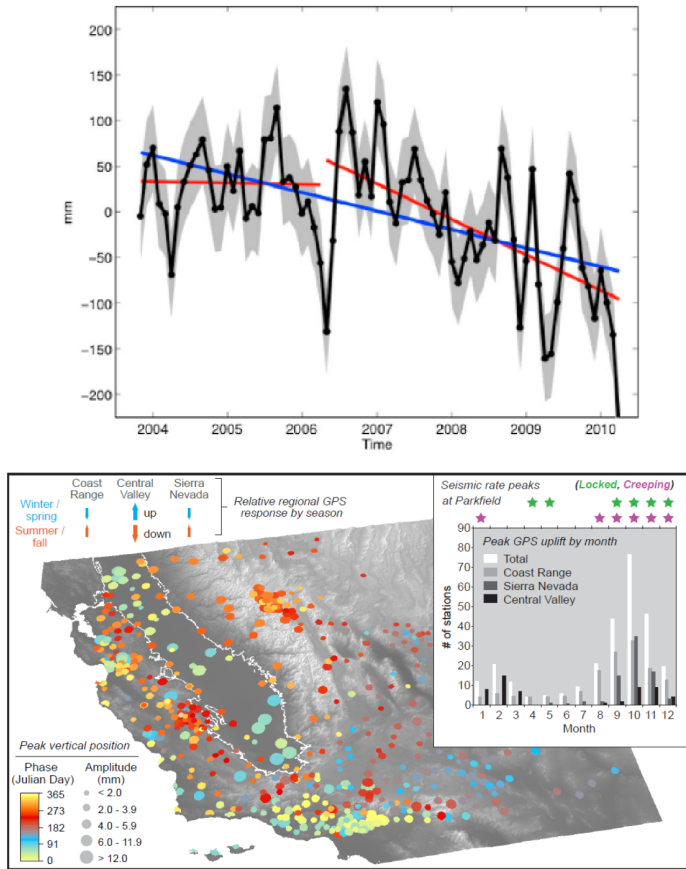


Figure 1. (top) Estimate of groundwater storage in Central Valley from GRACE gravity data and hydrological models [Famiglietti *et al.*, 2011]. Yearly load cycles are of order 10 cm or 1 kPa normal load. (bottom) GPS measured seasonal vertical motions in Sierra Nevada and Coast Ranges produced by seasonal surface loads showing 1-10 mm annual peak-to-peak amplitude [Amos *et al.*, 2014]. GPS measured seasonal motions in Sierra Nevada and Coast Ranges are anti-correlated with vertical motions Central Valley produced by poroelastic stress associated with seasonal groundwater level changes. The inset shows histograms of peak uplift phase (binned by month) for stations in the San Joaquin Valley, Sierra Nevada, and Coast Range. Peaks in seismicity rate for the locked and creeping San Andreas Fault at Parkfield are defined as months with higher than average declustered seismicity [Christiansen *et al.*, 2007].

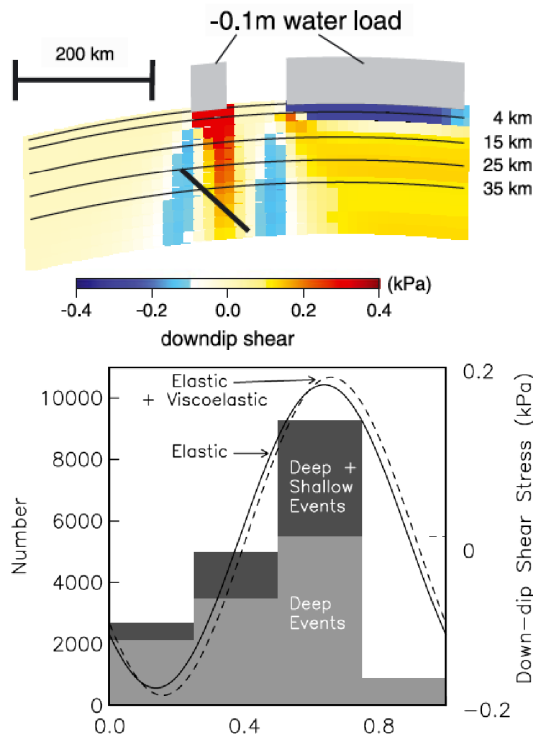


Figure 2. (top) Vertical cross-section of down-dip shear stress across southern Vancouver Island. The tremor producing transition zone from 25–55 km depth is indicated with the black line segment. Vertical exaggeration is a factor of 3.33. (bottom) Histogram of tremor occurrence binned by quarter of the year using the 2006-2011 catalog of events from British Columbia and northern Washington from Wech. Values from 0 to 1 on the x-axis span an entire year. Results are shown for all events and deep (> 40 km) events. Superimposed is the time-dependent down-dip shear stress at 45 km depth based on the model of annual hydrologic loading shown above. Both the elastic and summed elastic and viscoelastic components of the model predictions are shown. From Pollitz *et al.* [2013].

earthquake. In central California, seasonal cycles of snow and water loads in the Sierra Nevada and Central Valley lead to seasonal cycles in vertical position time series (Figure 1) and produce normal-stress variations of up to ~ 2 kPa on faults of the SAF system [Amos *et al.*, 2014], which may help drive observed seasonal seismicity patterns [Christiansen *et al.*, 2007]. As for the shorter-period loads, deep-seated slow slip and tremor appear to be particularly sensitive to seasonal modulation [Lowry, 2006; Pollitz *et al.*, 2013b, Figure 2].

Earth's pole tides involve annual and 14.24-month Chandler wobble periods, which are related to the nutation of Earth's axis of rotation relative to the solid earth. Stress cycles produced by the pole tides are of similar order of magnitude (~ 0.1 -10 kPa) as lunar tides, hydrological loads and atmospheric pressure cycles, and have been proposed to modulate tremor and slow-slip episodes in Cascadia and other subduction zones [Shen *et al.*, 2005]. Longer-period cycles of several years in the occurrence of large earthquakes have also been proposed, possibly involving very long-period tidal, atmospheric or oceanographic forcing mechanisms [e.g., Kilston and Knopoff, 1983; Tanaka, 2014 and references cited therein]. Finally, climate cycles associated with Earth's ice ages have been suggested to modulate earthquake occurrence via the substantial changes in stress associated with the flexural loads of large ice caps and changes in sea level over geologic time scales [e.g., Grollmund and Zoback, 2000; Ivins *et al.*, 2003; Luttrell and Sandwell, 2010].

Here, we explore seismicity catalogs spanning 12 to 26 years in central California, for periodic occurrence in earthquake frequencies at periods ranging from about 2 months to 11.5 years. We use the Schuster spectrum, Schuster periodogram, and multi-frequential periodogram analysis [Duttilleul, 2001] to evaluate if statistically significant periodicities can be identified considering both the full and declustered versions of the event catalogs. We test to what degree the periodic behavior of earthquakes in our target regions can be correlated with time series of periodic stress from semi-annual and annual tides, pole tides and seasonal hydrospheric surface loads by modeling the deformation associated with these loading cycles. To further explore the seasonal stress variation we evaluate the stress changes for California faults by considering the contribution of seven periodic loads (atmosphere, Earth pole tides, Earth tides, non-tidal ocean, ocean tides, temperature variations, and water storage). The deformation is resolved for major faults throughout northern California to assess the spatial temporal contributions of the load contributions.

2. Statistical Methods

Rigorous statistical analysis is required to document resolvable and significant periodicities of seismicity and correlation of earthquakes with modeled periodic sources of stress. A total of seven statistical analyses are performed sequentially, some in the frequency domain (periodogram analysis, spectral analyses) and others in the time domain (trigonometric model fittings, correlation analyses). The sequence of their application corresponds to the following steps: (i) detection of periodic components in time series using periodogram analysis [Duttilleul, 2001]; (ii) assessment of the periodicities detected, by the fitting of a relevant trigonometric model to the observed time series (with modification of the fitting procedure if the error term is found to be temporally autocorrelated); and (iii) validation of the periodic occurrence of earthquakes found, with various correlation analyses between predicted time series made of one, two or three periodic components for monthly earthquake frequencies and time series of periodic stress from semi-annual and annual tides, pole tides and seasonal hydrospheric loads. The description of the statistical methods below includes key references as well as the software to be

used for their implementation in our study.

2.1 Multi-frequential periodogram analysis

The multi-frequential periodogram statistic, $I^M(\omega)$ [Dutilleul, 2001], can be seen as an extension or a generalization of Schuster's (classical) uni-frequential periodogram, $I^C(\omega)$ [Schuster, 1897], for the following reasons. Let \mathbf{y} denote the $n \times 1$ vector containing the time series data $y(t)$ ($t = 1, \dots, n$), to be analyzed for periodicity analysis in the frequency domain. If $\mathbf{X}(\omega)$ ($0 < \omega < \pi$) is the matrix with n rows and 2 columns made of the cosine and sine values for angular values $\omega.t$ ($t = 1, \dots, n$), then $I^C(\omega) = \frac{2}{n} \mathbf{y}' \mathbf{X}(\omega) \mathbf{X}(\omega)' \mathbf{y}$, where $'$ denotes the transpose

operator of matrix algebra. At the Fourier frequencies $\omega_p = \frac{2.\pi.p}{n}$, $I^C(\omega)$ is exactly equal to the

sum of squares of the trigonometric model with one cosine wave at frequency ω_p and the companion sine wave, fitted by ordinary least squares (OLS) to the time series \mathbf{y} ; at non-Fourier frequencies, the equality is an approximation [Brillinger, 1981]. By comparison, with $0 < \omega_1 < \dots < \omega_K < \pi$ (K , a strictly positive integer smaller than $\frac{n}{2}$) so that $\omega = (\omega_1, \dots, \omega_K)$, $I^M(\omega) = \mathbf{y}'$

$\mathbf{X}(\omega) (\mathbf{X}(\omega)' \mathbf{X}(\omega))^{-1} \mathbf{X}(\omega)' \mathbf{y}$, where $^{-1}$ denotes the inverse operator for a square matrix of full rank. Even when ω_k ($k = 1, \dots, K$) are not Fourier frequencies, the value of $I^M(\omega)$ is exactly the sum of squares of the trigonometric model with K cosine waves and the companion sine waves,

fitted by OLS to the time series; when $K = 1$ and $\omega_1 = \frac{2.\pi.p}{n}$ for some integer p between 1 and

$$\frac{n}{2}, I^M(\omega_1) = I^C(\omega_1).$$

Mathematical, statistical and computational details about the method of multi-frequential periodogram analysis (MFPA) can be found in Dutilleul [2001]. In summary, three particularly important properties or features of $I^M(\omega)$ and its analysis are: (i) in general conditions, the $I^M(\omega)$ statistic follows a chi-square distribution with $2K$ degrees of freedom; (ii) a stepwise procedure, which includes a test of significance at each step, is available to estimate the number of periodic components in the time series; and (iii) the maximization of $I^M(\omega)$ for a given number K , which is performed as part of the stepwise procedure, is effective whether the spectrum of the stochastic process underlying the time series is discrete (i.e. without autocorrelation) or mixed (i.e. the process possesses an autocorrelation function in addition to a mean function that can be modeled with a number of periodic components in the form of cosine-sine waves). *MFPA.m*, a customized MATLAB (The MathWorks, Inc., Natick, MA) function, which comes with Dutilleul [2011], was used for the MFPA performed in our study.

2.2 Trigonometric model fitting

Annual tides, pole tides and seasonal hydrospheric loads all have 12-month periodicities, and the pole tides are dominated by a period of 433 days (12.24 months). Thus, in the areas where the MFPA results justified it (i.e. when MFA-estimated periods were close to 12 or 14.24 months), two trigonometric models, one with 4-, 6- and 12-month cosine and sine waves and the other with 12- and 14.24-month cosine and sine waves were fitted to the time series of monthly earthquake frequencies, for the detection of peaks in seismicity at these periods and further comparisons and correlation analyses. Model fitting was performed by least squares, ordinary

least squares (OLS) when no temporal autocorrelation was found in OLS residuals and otherwise by generalized least squares (GLS). The software used for this was SAS (Statistical Analysis System), Version 9.3 (32), in particular its procedures GLM, (OLS model fitting), AUTOREG (GLS model fitting) and ARIMA (analysis of temporal autocorrelation of OLS residuals). The statistical indicators of model performance were: the R-square (ratio of model sum of squares to total sum of squares) and the probability of significance of the F -test of significance for it; and the sign and value of the cosine and sine coefficient estimates and the probability of significance of the t -tests of significance for them.

2.3 Cross-correlation analysis with modeled periodic loads

In order to resolve correlations between periodic (or frequency) components, we examine ‘spectral correlations’ via squared coherency analysis and cross-spectrum phase analysis. The coherency analysis determines a squared correlation coefficient in the frequency domain, thus showing the degree of similarity (from 0, lowest, to 1, highest) of the fluctuations in time of the two time series compared at the period/frequency considered. The phase analysis indicates the shift, between peaks/troughs in one time series and the other at the period/frequency considered. The SAS procedure SPECTRA is used for these two spectral analyses, with a (1, 2, 1) triangular window. The statistical analyses employ the Kendall’s tau rank-based correlation statistic, evaluated in the time domain between an observed time series of monthly earthquake frequencies and the time series predicted from the considered periodic components. The SAS procedure used is PROC CORR, option KENDALL, with the objective to assess the concordance between the two time series involved.

3. Statistical Significance of Detected Periodicity in CA Earthquake Occurrence

We rely on the ANSS (Advanced National Seismic System) composite catalog accessed via the Northern California Earthquake Data Center (<http://www.ncedc.org/anss/catalog-search.html>), which incorporates data from all regional catalogs and removes duplicate solutions for the same event. The magnitude of completeness M_c , above which a catalog is understood to capture all events, is temporally and spatially variable across California depending on the spacing of seismic stations [Wiemer and Wyss, 2000]. We use a lower magnitude threshold ($M_{2.5}$) in our search areas that is somewhat higher than M_c to avoid temporal variations related to changes in the seismic network. As a number of large earthquakes (e.g., 2003 San Simeon, 2004 Parkfield) occurred in our study region, we also consider sub-catalogs for which we exclude time intervals spanning these events and their initial aftershocks.

To ensure a robust analysis we test 26 years of $M \geq 2.5$ catalog data and apply two declustering methods. The first is the [Reasenber, 1985] method developed for northern and central California. The second is a spatial-temporal ETAS model that estimates the probability that an event is a background earthquake [Zhuang *et al.*, 2002]. The two algorithms are point process statistical models that uniquely classify earthquake families and background events. Reasenber [1985] determines the statistical significance of earthquake pairs in space and time for a mainshock/aftershock relationship following Omori’s Law as well as the inclusion of foreshocks into a cluster family. The classification process in this declustering algorithm is dependent on model input parameters to establish a spatiotemporal relationship between two events. The identified cluster families are replaced with a single event resulting in a temporally stationary process, but does not address higher order sequences, such as seismic swarms, when linking earthquakes to a single mainshock. The second declustering method we consider is a

space-time version of the epidemic-type aftershock sequence (ETAS) model [Ogata, 1992] that, for each earthquake, calculates the probability of being a background event [Zhuang *et al.*, 2002]. Establishing the background intensity with an ETAS model allows the use of a non-parametric, stochastic declustering based on the probability of each event contributing to the background rate. The resulting declustered catalog is a non-unique product, due to the stochastic nature, to classify more earthquakes in a cluster sequence. The removal of any event from an earthquake catalog is non-trivial and requires extensive consideration when interpreting seismicity results. Results for one region in the study area are shown in Figure 3.

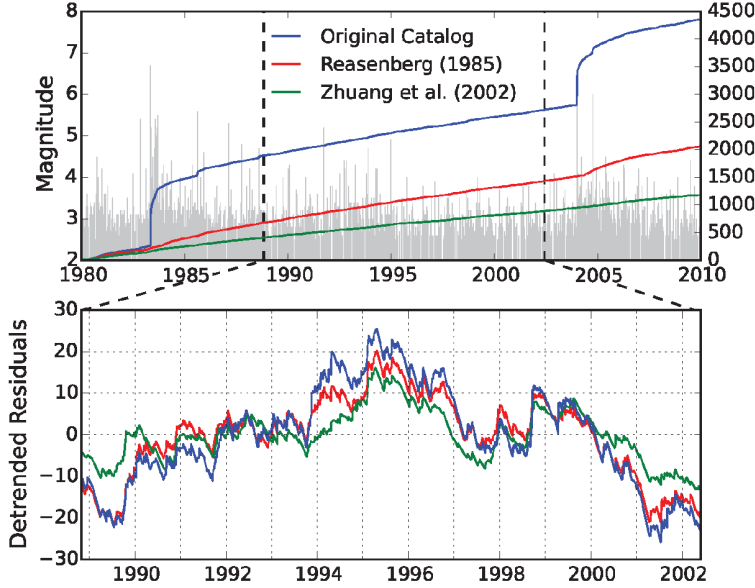


Figure 3. (top) Seismicity between 1980 and 2010, within the CSAF-PKD region shown in Figure 4. Event magnitude is represented in gray. The original catalog contains 4352 events with $M \geq 2.5$, plotted cumulatively in the blue curve. The red curve represents the declustered seismicity obtained using the *Reasenber* [1985] algorithm, with 53% of the events removed. The green curve is for the declustered seismicity resulting from the *Zhuang et al.* [2002] algorithm and removal of 73% of the events. (bottom) Curves representing the deviations from linear trends fitted to the data. To avoid effects from major aftershock sequences, events from 1 October 1988–31 May 2002 are used in the comparison of original and declustered data.

Both declustering methods are widely used and appropriate for the purpose of testing the regions of interest. We consider both the original earthquake catalogs as well as subsets made of declustered events that separate dependent seismic activity produced by fault interaction, including foreshocks and aftershocks, from independent background earthquakes, including mainshocks and single events [van Stiphout *et al.*, 2012], thereby testing a total of six catalogs. We examine to what degree the choice of declustering algorithm [Reasenber, 1985; Zhuang *et al.*, 2002] affects the results of our analysis.

We explore two regions of CA, one near the central SAF and the second in the Sierra Nevada – Eastern California Shear Zone (SN-ECSZ), for periodic behavior considering periods of 2 months up to multiple years using three independent statistical tests. We chose the first test area to be representative of the seismicity along the SAF and adjoining transpressional Coast Ranges near where *Christiansen et al.* [2007] previously reported annual modulation. The second region includes the seismically most active section of the ECSZ.

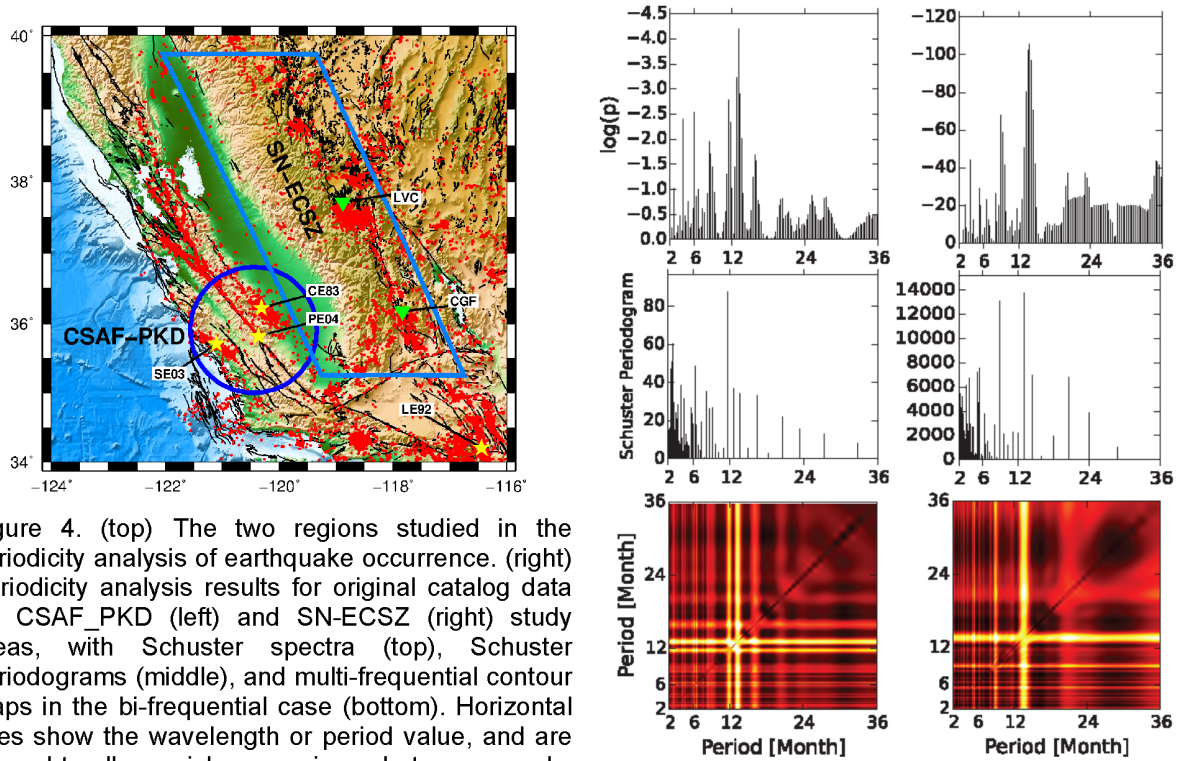


Figure 4. (top) The two regions studied in the periodicity analysis of earthquake occurrence. (right) Periodicity analysis results for original catalog data for CSAF-PKD (left) and SN-ECSZ (right) study areas, with Schuster spectra (top), Schuster periodograms (middle), and multi-frequential contour maps in the bi-frequential case (bottom). Horizontal axes show the wavelength or period value, and are aligned to allow quick comparisons between panels, from top to bottom. The three statistical tests indicate a significant period at 12-months. Shown here are the original catalog data and similar results are found when using the declustered data sets.

The statistical analyses are described in Section 2 and more details are provided in [Duttilleul *et al.*, 2015]. In the point-pattern approach that is using sequences of earthquake dates, the Schuster spectrum is computed between a minimum period and a maximum period to be tested. In the time-series approach, the uni-frequential Schuster periodogram and the multi-frequential periodogram analysis (MFPA) are applied to monthly earthquake numbers. We confirm that the Schuster periodogram is a very basic spectral tool and its use should be limited to very simple situations, i.e., a single periodicity with one main frequency and harmonics. We find the MFPA provides better documentation on the periodicities detected and recommend the application of the MFPA method in seismological studies aimed at the detection of periodicities in earthquake occurrence, in combination with the Schuster test and spectrum.

Near Parkfield, CA we find strong evidence for annual periods in earthquake occurrence, consistent with previous results suggesting seasonal modulation of seismicity [Christiansen *et al.*, 2007]. Shown in Figure 4 are the results indicating statistically significant periods of about 4-, 6-, and 12-months for seismicity located on the SAF near Parkfield. For this region we find peak earthquake occurrence in the dry fall months of August and September and a secondary peak in activity in April. Similarly, in the SN-ECSZ we find a statistically significant annual period, as well as a ~ 14 month period that we specifically test for in order to consider the period of pole-tide induced stresses. The results indicate the declustering methods reduce the periodic component resolved in the time series, but do not produce a Poissonian process since we are able to resolve similar periods when compared to the original time series.

From a seismological perspective, we find that there is significant annual periodicity in earthquakes along the central SAF and adjacent Coast Ranges that appears to reflect seasonal loading from hydrospheric and tidal loads. The modulation of seismicity with a period of one-year supports our hypothesis of seasonal loading and warrants our continued efforts to model the seasonal deformation associated with these time varying loads. The statistical work researching the periodicities in California and the exploration of tidal stresses is published in the Journal of Geophysical Research: Solid Earth [Duttilleul *et al.*, 2015].

4. Time Varying Stress Modeling

Sources of loading investigated in this study include: atmospheric pressure, Earth pole tides, Earth tides, non-tidal ocean loading, ocean tidal loading, surface temperature, and water storage. The loading contributions are considered independently to obtain an accurate estimate of the magnitude of each. The deformation associated with the loading sources are calculated at for the region $34^{\circ}\text{N} - 42^{\circ}\text{N}$ and $124^{\circ}\text{W} - 116^{\circ}\text{W}$ from 2006 – 2014. Two techniques are employed to model the deformation. For the Earth body tides, Earth pole tides, and temperature variations we use theoretical models to estimate the deformation. For changes in the atmospheric, non-tidal ocean, ocean tidal, and surface water stresses we utilize a general loading model for a spherical layered Earth. The loading model is a modified version of STATIC1D for a vertical loading force [Pollitz, 1996; Pollitz *et al.*, 2013a]. We assume a 1D preliminary reference Earth structure (PREM) and model deformation at 8 km depth to represent the seismogenic zone. Assuming isotropic elasticity the stresses are calculated using a Poisson ratio of 0.25 and a shear modulus of 30 GPa. Using the models described, a deformation time series is calculated for every fault location in the study from 2006 – 2014, which is determined by the period of the continuous GPS network. We report results for the two profiles across the study area that include locations of the periodicity study outlined in Figure 4.

4.1 Atmospheric pressure

The atmospheric loading contribution is obtained from the Global Geophysical Fluid Center (<http://geophy.uni.lu/ncep-loading.html>) [van Dam, 2010] for a global grid derived from the National Center for Environmental Protection reanalysis surface pressure data set. Three dimensional displacements are calculated following Van Dam and Wahr [1987]. The input loads are estimated on a 0.5° grid for the region $30^{\circ}\text{N} - 44^{\circ}\text{N}$ and $124^{\circ}\text{W} - 114^{\circ}\text{W}$. This is the same data set used to correct the GPS time-series used in this study, as described below. The load is discretized in a 0.25° grid and the deformation at seismogenic depth is calculated using the general loading model.

4.2 Earth pole-tides

Changes in the Earth's rotation pole axis produce observable surface deformation and theoretical calculations can estimate the horizontal and radial displacements [Wahr, 1985]. Earth's pole tides involve annual and 14.24-month Chandler wobble periods, which are related to the nutation of Earth's axis of rotation relative to the solid earth. The displacements can be extended to estimate the Earth pole tide induced strains using equations 1-3 [Shen *et al.*, 2005].

$$\varepsilon_{\theta\theta} = 2l \frac{\Omega_0^2 r}{g} [\sin 2\theta (m_x \cos \lambda + m_y \sin \lambda) - m_z \cos 2\theta] \\ - h \frac{\Omega_0^2 r}{2g} [\sin 2\theta (m_x \cos \lambda + m_y \sin \lambda) - m_z \sin^2 2\theta] \quad (1)$$

$$\varepsilon_{\lambda\lambda} = l \frac{\Omega_0^2 r}{g} [\cot \theta (1 - \cos 2\theta)(m_x \cos \lambda + m_y \sin \lambda) - m_z \sin 2\theta] \\ - h \frac{\Omega_0^2 r}{2g} [\sin 2\theta (m_x \cos \lambda + m_y \sin \lambda) + 2m_z \sin^2 \theta] \quad (2)$$

$$\varepsilon_{\theta\lambda} = -l \frac{\Omega_0^2 r}{g} [\sin \theta (m_x \sin \lambda + m_y \cos \lambda)] \quad (3)$$

Where l and h are the Love numbers ($l = 0.085$; $h = 0.600$), Ω is the rotation rate, r is the position radius, g is the gravitational acceleration, λ is the longitude, θ is the colatitude, m_x and m_y are the vectors components of the change in the rotation pole, and m_z is the change in the rotation rate. Note the change in rotation rate is insignificant compared to the variations in the rotation pole [Wahr, 1985]. The rotation pole vector components and rotation rate changes are obtained from the International Earth Rotation and Reference System Service (<https://www.iers.org/IERS/EN/DataProducts/EarthOrientationData/eop.html>). The Earth orientation parameters are smoothed values at 1-day intervals and are calculated with respect to the IAU2000A nutation model, which is consistent with ITRF-2008. The natural period of the pole-tide induced deformation is ~ 12 and ~ 14.2 months. The wavelength of these tides is on the order of 20000 km, resulting in approximately the same tidal loading experienced at each study area.

4.3 Earth tide

The interaction of celestial bodies deforms the solid Earth and induces changes in the gravitation potential (see Agnew [2015] for a complete review of tidal forces). The solid Earth tides are the resulting displacements from this interaction and are derived assuming an oceanless Earth. The ocean tidal loading is considered separately when using this framework. Theoretical Earth body tide strains are calculated using the SPOTL software package [Agnew, 1997] for a 1 hour time step. The largest tidal displacements are observed in the diurnal tidal signal. For this study we are interested in the long period deformation and filter the time series to retain the annual component.

4.4 Non-tidal ocean

The non-tidal ocean load results in deformation associated with the changes in the distribution of water mass due to Earth tides and atmospheric forcing. The load is equivalent to the change in the pressure exerted on the seafloor by the mass of a column of water directly above. The monthly data product is calculated by the ECCO Project (<http://www.ecco-group.org>)

and available through the Jet Propulsion Laboratory (ftp://podaac-ftp.jpl.nasa.gov/allData/tellus/L3/ecco_obp/). The ocean model is the same correction applied to the GPS time series.

4.5 Ocean tide

As described for the Earth tides, changes in gravitational potential deform the Earth. The tidal oscillation of the oceans is dominated by the semidiurnal and diurnal tidal species [Agnew, 2015]. The tidal loading prediction used is the TPXO7.2 model calculated on a 0.25° global grid [Egbert and Erofeeva, 2002]. The data product is available through the Oregon State University TOPEX/Poseidon Global Inverse Solution (volkov.oce.orst.edu/tides/global.html). The ocean tide model is the same correction applied to the GPS time series. This study is interested in the long period annual tidal changes and the time series are filtered to retain only this component.

4.6 Temperature

Seasonal temperature variations at the Earth surface induce thermoelastic expansion in competent surface geology that induce strains into the crust [Berger, 1975]. Assuming a two dimensional elastic half space the expected strain value can be quantified using reasonable homogenous elastic parameters [Ben-Zion and Leary, 1986; Tsai, 2011]. The largest thermoelastic perturbation is expected near the surface as the thermoelastic strain decays with depth [Tsai, 2011]. Temperature data is acquired from the North America Land Data Assimilations System (ldas.gsfc.nasa.gov/nldas/). Hourly temperatures are averaged to daily values on a 0.125° grid for the region 34°N – 42°N and 124°W – 116°W from 2006 – 2014. The thermoelastic strains are estimated using equations 4-7. The equations are fully described in Tsai [2011].

$$A(t) = \frac{1+v}{1-v} k\alpha T_0 \sqrt{\frac{\kappa}{\omega}} e^{-\sqrt{\frac{\omega}{2\kappa}} y_b} \cos\left(\omega t - \sqrt{\frac{\omega}{2\kappa}} y_b \frac{\pi}{4}\right) \quad (4)$$

$$\varepsilon_{xx}(x, y, t) \approx A(t) \sin kx e^{-ky} [1(1-v) - ky] \quad (5)$$

$$\varepsilon_{yy}(x, y, t) \approx -A(t) \sin kx e^{-ky} [2v - ky] \quad (6)$$

$$\varepsilon_{xy}(x, y, t) \approx A(t) \cos kx e^{-ky} [1 - ky] \quad (7)$$

Where v is the Poisson ratio ($v=0.3$), k is the horizontal wave number ($k = 2\pi / 10e3$), α is the coefficient of linear thermal expansion ($\alpha = 1e-05 \text{ } ^\circ\text{C}^{-1}$), T_0 is the annual temperature amplitude (half the peak-to-peak temperature), κ is the thermal diffusivity ($\kappa=1e-06 \text{ m}^2 \text{ s}^{-1}$), ω is the frequency ($\omega=2e-07 \text{ s}^{-1}$), and y_b is the incompetent layer thickness at the surface ($y_b = 0.5 \text{ m}$). The thermoelastic strains are sufficient to estimate the deformation and additional parameter constraints are required to further improve the modeling.

4.7 Water Storage

Precipitation in California follows an annual cycle with dry summer months followed by wet winter months when ground water is replenished and snow pack accumulates in the mountains. The monthly water storage in the study area is estimated using the vertical displacements recorded by continuous GPS stations in the Plate Boundary Observatory network.

The assumptions for this procedure is that water mass is modulating the seasonal displacements on the Earth surface after the removal of additional loading sources from the GPS time series. This study uses the GPS daily solutions processed with GIPSY software in Point Processing mode [Zumberge *et al.*, 1997] by the Jet Propulsion Laboratory and corrected for ocean tidal loading [Lyard *et al.*, 2006] using a consistent reference frame [Fu *et al.*, 2012]. The GPS solutions are transformed into the ITRF2008 reference frame. As detailed in this section the atmospheric loading components are a source of seasonal deformation and are removed from the GPS solutions in the postprocessing in order to retain the hydrological loading signal.

Using $0.25^\circ \times 0.25^\circ$ grid patches for the study area we resolve the time-varying terrestrial water storage as a function of the vertical displacements. The study area contains 773 GPS stations and we remove 72 stations that display a large subsidence signal due to groundwater extraction in agricultural areas. The criteria from removal is a stations that exhibits large uplift in the winter and subsidence in the summer, thereby out of phase with the precipitation and following the patterns of anthropogenic pumping. The surface deformation is translated to a mass load using Green's functions for a spherical gravitating Earth model [Farrell, 1972] assuming an elastic response to water storage variations [Argus *et al.*, 2014; Fu *et al.*, 2015], which represents the mass change in the hydrosphere. We solve for the water storage using a weighted least-square smoothed inversion method by minimizing equation 8.

$$\min \{ \|W(Gx - b)\|^2 + \beta^2 \|Lx\|^2 \} \quad (8)$$

Where G is the Green's functions for a $m \times n$ matrix (m is the number of GPS stations and n is the number of patches), x is the load mass change, b is the observed displacement, L is the Laplacian smoothing operator, W scales the residuals, and β adjusts the residual misfit.

5. Stress Changes on California Faults

The results are presented as individual stress change contributions for each of the eight loads of interest and as a combined seasonal deformation time series. The results are resolved as a shear, normal and Coulomb ($\mu=0.4$) stress time-series using the geometry described in the Uniform California Earthquake Rupture Forecast (UCERF3) model [Field *et al.*, 2013]. The results are shown for six faults (Table 1) along two profiles that extend 300 km across the study area. The time series of the six locations are shown in Figure 5 and 6. The faults selected are representative of the structure geometry as it changes across the region. For the southern portion of the study area the locations shown are Oceanic Fault Zone near San Simeon, CA, the central San Andreas Fault near Parkfield, CA, and the Owens Valley Fault, Keough Hot Springs section. In the northern region of the study area the locations are the San Andreas Fault near Bodega Bay, CA, the Foothill Fault System east of Sacramento, CA in the Sierra Nevada range front, and the North Tahoe Fault near Truckee, CA.

Southern Profile

The Oceanic Fault Zone is an oblique reverse fault system near San Simeon, CA. The average peak-to-peak shear stress and normal stress change is ~ 1.25 kPa and ~ 1.0 kPa, respectively. The greatest shear stress is from the annual ocean tide, which constitutes the majority of the signal. The largest contribution to the normal stress is the atmosphere loading that is ~ 0.6 kPa change per year. The annual peak-to-peak Coulomb stress change is ~ 2 kPa.

The central San Andreas Fault is a vertically dipping right-lateral strike-slip fault and is

shown near Parkfield, CA section. The average peak-to-peak shear and normal stress change is ~ 0.75 kPa and ~ 3.0 kPa, respectively. Note the average shear stress changes in time due to the phase difference of the combined loads. The two largest loading components are the temperature (~ 12 month period) and the Earth pole time (~ 12 and 14.2 month period) and are out of phase from 2011 – 2015. The largest load for the normal stress change is the water storage. The peak-to-peak Coulomb stress is ~ 1.25 kPa and decreases when the shear stress change is at a minimum.

In the eastern California shear zone is the Owens Valley Fault in the foothills of the eastern Sierra Nevada. The fault system contains normal and strike-slip fault geometry. The Keough section of the Owens Valley Fault is a normal fault near Bishop, CA. The average peak-to-peak shear and normal stress is ~ 1.0 kPa and ~ 1.0 kPa, respectively. The shear stress change is controlled by the seasonal water storage. Interestingly, the normal stress changes from each load is < 0.5 kPa but are in phase to produce a ~ 1 kPa stress change. The peak-to-peak Coulomb stress change is < 0.5 kPa. The shear and normal stress time series are out of phase and the resulting Coulomb stress change is minimal.

Northern profile

The northern San Andreas Fault near Bodega Bay, CA is a vertically dipping right lateral strike-slip fault and is near the coastline for much of northern CA. The peak-to-peak shear and normal stress change is ~ 0.75 kPa and ~ 2.0 kPa, respectively. Similar to the central fault section the shear stress is modulated by the Earth pole tide. The largest normal stress contribution is from the annual ocean tides. The peak-to-peak Coulomb stress change is ~ 1.0 kPa.

The Foothills Fault system is a series of normal faults in the western foothills of the Sierra Nevada. The peak-to-peak shear and normal stress change is < 0.25 kPa and ~ 2.0 kPa, respectively. None of the loading contributions indicate a significant shear stress change. Similarly the Coulomb stress indicates < 0.5 kPa through the time series.

The North Tahoe Fault system is a normal fault in the Sierra Nevada along the Tahoe range front. The peak-to-peak shear and normal stress change is ~ 2.0 kPa and ~ 2.5 kPa, respectively. The greatest stress contribution for both the shear and normal components is from the water storage, notably snow for the location. The shear and normal stress are out of phase and the resulting peak-to-peak Coulomb stress change is ~ 0.5 kPa.

Table 1. Fault geometry for selected locations in the study area.

Southern Profile	Lon	Lat	Strike	Dip	Rake
Oceanic fault zone, San Simeon	-121.18	35.67	312	58	135
Parkfield near creep/lock section	-120.56	36.00	320	90	180
Owens Valley Fault	-118.38	37.24	340	50	-90
Northern Profile	Lon	Lat	Strike	Dip	Rake
SAF, Bodega Bay	-123.80	39.15	325	90	180
Foothill fault system	-121.46	39.53	333	60	-90
North Tahoe Fault	-119.96	39.32	17	50	-90

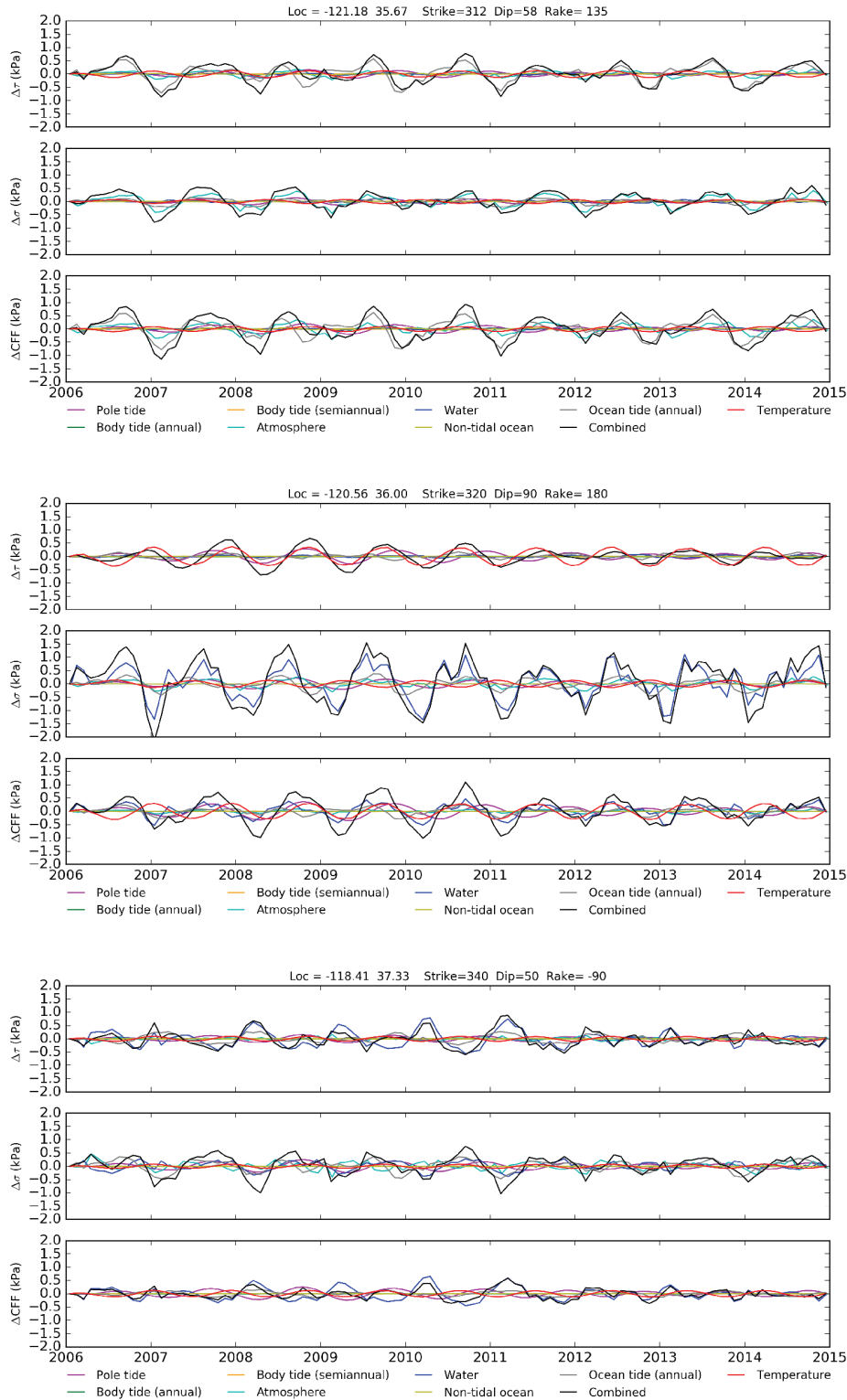


Figure 5. Stress curves for locations listed in Table 1. (top) San Simeon, CA. (middle) Parkfield, CA. (bottom) Owens Valley, CA. Each panel contains 9 time series indicated by color for the different loading sources. Each location shows the shear, normal, and Coulomb ($\mu=0.4$) stress. The locations and fault geometry for the stress curves is indicated at the top. The black curve is the combined stress for all 8 loads.

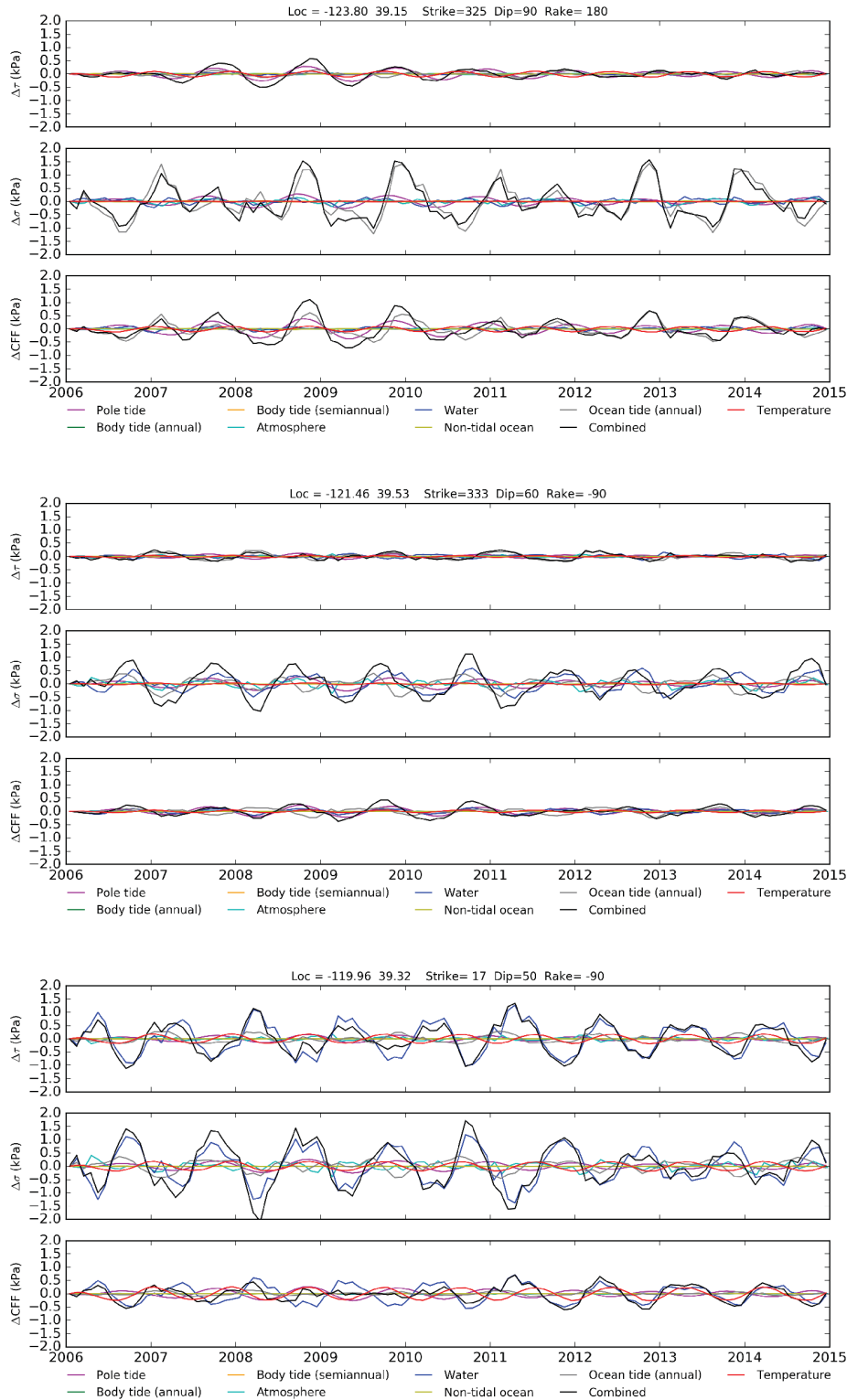


Figure 6. Stress curves for locations listed in Table 1. (top) SAF at Bodega Bay, CA. (middle) Foothill Faults, CA. (bottom) North Tahoe, CA. Each panel contains 9 time series indicated by color for the different loading sources. Each location shows the shear, normal, and Coulomb ($\mu=0.4$) stress. The locations and fault geometry for the stress curves is indicated at the top. The black curve is the combined stress for all 8 loads.

6. Seismicity Analysis with Seasonal Loads

We explore the phase and amplitude information of periodic sources of stress. In all locations presented the pole tide, body tide, non-tidal ocean, temperature, and atmosphere are the lowest stress amplitudes. Locations near the coast show a larger ocean tide stress for the normal component (Figure 5 and 6 top panel). For all inland locations the largest stress contribution is the seasonal hydrological loading. This is most prominent in the Sierra Nevada North Tahoe Fault system, however the shear and normal stress are out of phase to increase the Coulomb failure stress for normal faults in this location. The modeled peak-to-trough Coulomb stress amplitudes on the central SAF and coastal oblique faults is ~ 1.5 kPa. On the central SAF the hydrological normal stress unloading is ~ 1.25 kPa and is the largest amplitude stress resolved. Normal-stress cycles from seasonal unloading are estimated to be of order ~ 1.5 kPa peak-to-trough, with greatest tensile stress in October during the drier months. In the seismicity analysis, we exclude events the Geysers and Long Valley geothermal and volcanic centers where variation in the seismicity is mainly a response to large volume fluid injection [Johnson *et al.*, 2016] or the upwelling of volcanic fluids. Analysis of earthquake focal mechanisms from 2006 - 2014 reveals more earthquakes occurring during the slip-encouraging stress conditions that vary as a function of space, time, and fault geometry [Johnson *et al.*, 2016 in review]. We find a strong correlation for oblique and dip-slip events occurring during fault unclamping. The strike-slip events appear to occur more frequently during positive shear stress loading. We are able to resolve excess seismicity from a 1-5 kPa Coulomb stress change, which requires an optimal orientation and in-phase timing to constrain a seasonal mechanical response. This suggests that the fall peak in earthquake occurrence is due to the dominantly fault-normal stress cycles of hydrological surface loads, while the second peak in the spring may be related to stress cycles from the pole-tide and tidal contributions, which indicate a peak shear stress in March and September. The occurrence of two peaks in seismicity for regions of the central Coast Ranges is not fully explained by the stress conditions favorable for slip dominated by the hydrological unloading, suggesting contributions from the other annual load processes. We infer that earthquake populations are modulated at periods of natural hydrological loading cycles.

7. Bibliography

- Duttilleul, P., C. W. Johnson, R. Bürgmann, Y. Wan, and Z.-K. Shen (2015), Multifrequential periodogram analysis of earthquake occurrence: An alternative approach to the Schuster spectrum, with two examples in central California, *Journal of Geophysical Research: Solid Earth*, *120*(12), 8494-8515, doi:10.1002/2015JB012467.
- Johnson, C. W., E. J. Totten, and R. Bürgmann (2016), Depth migration of seasonally induced seismicity at the Geysers geothermal field, *Geophys. Res. Lett.*, *43*(12), 6196-6204 doi:10.1002/2016GL069546.
- Johnson, C. W., Y. Fu, and R. Bürgmann (2016), Seasonal water storage, stress modulation and California seismicity *Science*, in review.

References

- Agnew, D. C. (1997), NLOADF: A program for computing ocean-tide loading, *Journal of Geophysical Research*, 102(B3), 5109-5110, doi:10.1029/96jb03458.
- Agnew, D. C. (2015), 3.06 - Earth Tides A2 - Schubert, Gerald, in *Treatise on Geophysics (Second Edition)*, edited, pp. 151-178, Elsevier, Oxford, doi:10.1016/B978-0-444-53802-4.00058-0.
- Amos, C. B., P. Audet, W. C. Hammond, R. Bürgmann, I. A. Johanson, and G. Blewitt (2014), Contemporary uplift and seismicity in central California driven by groundwater depletion, *Nature*, *in press*, doi:10.1038/nature13275.
- Argus, D. F., Y. Fu, and F. W. Landerer (2014), Seasonal variation in total water storage in California inferred from GPS observations of vertical land motion, *Geophysical Research Letters*, 41(6), 1971-1980, doi:10.1002/2014gl059570.
- Beeler, N. M., and D. A. Lockner (2003), Why earthquakes correlate weakly with the solid Earth tides: Effects of periodic stress on the rate and probability of earthquake occurrence, *Journal of Geophysical Research*, 108(B8), doi:10.1029/2001jb001518.
- Ben-Zion, Y., and A. A. Allam (2013), Seasonal thermoelastic strain and postseismic effects in Parkfield borehole dilatometers, *Earth and Planetary Science Letters*, 379, doi:10.1016/j.epsl.2013.1008.1024.
- Ben-Zion, Y., and P. Leary (1986), Thermoelastic strain in a half-space covered by unconsolidated material, *Bulletin of the Seismological Society of America*, 76(5), 1447-1460.
- Berger, J. (1975), A note on thermoelastic strains and tilts, *Journal of Geophysical Research*, 80(2), 274-277, doi:10.1029/JB080i002p00274.
- Bettinelli, P., J.-P. Avouac, M. Flouzat, L. Bollinger, G. Ramillien, S. Rajaure, and S. Sapkota (2008), Seasonal variations of seismicity and geodetic strain in the Himalaya induced by surface hydrology, *Earth and Planetary Science Letters*, 266, 332-344, doi:10.1016/j.epsl.2007.11.021.
- Bollinger, L., F. Perrier, J. P. Avouac, S. Sapkota, U. Gautam, and D. R. Tiwari (2007), Seasonal modulation of seismicity in the Himalaya of Nepal, *Geophysical Research Letters*, 34(8), doi:10.1029/2006GL029192.
- Chen, K. H., R. Bürgmann, and R. M. Nadeau (2013), Do earthquakes talk to each other? Triggering and interaction of repeating sequences at Parkfield, *Journal of Geophysical Research*, 118, doi:10.1029/2012JB009486.
- Christiansen, L. B., S. Hurwitz, and S. E. Ingebritsen (2007), Annual modulation of seismicity along the San Andreas Fault near Parkfield, CA, *Geophysical Research Letters*, 34(4), doi:10.1029/2006gl028634.
- Cochran, E. S., J. E. Vidale, and S. Tanaka (2004), Earth tides can trigger shallow thrust fault earthquakes, *Science*, 306, 1164-1166, doi:10.1126/science.1103961.
- Dong, D., P. Fang, Y. Bock, M. K. Cheng, and S. Miyazaki (2002), Anatomy of apparent seasonal variations from GPS-derived site position time series, *Journal of Geophysical Research: Solid Earth*, 107(B4), ETG 9-1-ETG 9-16, doi:10.1029/2001JB000573.

- Dutilleul, P. (2001), Multi-frequential periodogram analysis and the detection of periodic components in time series, *Communications in Statistics - Theory and Methods*, 30(6), 1063-1098, doi:doi:10.1081/STA-100104350.
- Dutilleul, P., C. W. Johnson, R. Bürgmann, Y. Wan, and Z.-K. Shen (2015), Multifrequential periodogram analysis of earthquake occurrence: An alternative approach to the Schuster spectrum, with two examples in central California, *Journal of Geophysical Research: Solid Earth*, 120(12), 8494-8515, doi:10.1002/2015JB012467.
- Egbert, G. D., and S. Y. Erofeeva (2002), Efficient Inverse Modeling of Barotropic Ocean Tides, *Journal of Atmospheric and Oceanic Technology*, 19(2), 183-204, doi:doi:10.1175/1520-0426(2002)019<0183:EIMOBO>2.0.CO;2.
- Ellsworth, W. L., M. V. Matthews, R. M. Nadeau, S. P. Nishenko, P. A. Reasenberg, and R. W. Simpson (1999), A physically-based earthquake recurrence model for estimation of long-term earthquake probabilities, *Workshop on earthquake recurrence: state of the art and directions for the future*, ING, Rome, 22-25 February, 1999.
- Farrell, W. E. (1972), Deformation of the Earth by surface loads, *Reviews of Geophysics*, 10(3), 761-797, doi:10.1029/RG010i003p00761.
- Field, E. H., et al. (2013), Uniform California earthquake rupture forecast, version 3 (UCERF3)—The time-independent model: U.S. Geological Survey Open-File Report 2013–1165, *California Geological Survey Special Report 228*, and *Southern California Earthquake Center Publication 1792*, 97p, <http://pubs.usgs.gov/of/2013/1165/>
- Freed, A. M. (2005), Earthquake triggering by static, dynamic, and postseismic stress transfer, *Annual Reviews of Earth and Planetary Sciences*, 33(doi:10.1146/annurev.earth.33.092203.122505), 335-368.
- Fu, Y., D. F. Argus, and F. W. Landerer (2015), GPS as an independent measurement to estimate terrestrial water storage variations in Washington and Oregon, *Journal of Geophysical Research: Solid Earth*, 120(1), 552-566, doi:10.1002/2014JB011415.
- Fu, Y. N., J. T. Freymueller, and T. van Dam (2012), The effect of using inconsistent ocean tidal loading models on GPS coordinate solutions, *Journal of Geodesy*, 86(6), 409-421, doi:10.1007/s00190-011-0528-1.
- Gao, S. S., P. G. Silver, A. T. Linde, and I. S. Sacks (2000), Annual modulation of triggered seismicity following the 1992 Landers earthquake in California, *Nature*, 406, 500-504.
- Grollimund, B., and M. D. Zoback (2000), Post glacial lithospheric flexure and induced stresses and pore pressure changes in the northern North Sea, *Tectonophysics*, 327(1-2), 61–81.
- Hainzl, S., Y. Ben-Zion, C. Cattania, and J. Wassermann (2013), Testing atmospheric and tidal earthquake triggering at Mt. Hochstaufen, Germany, *Journal of Geophysical Research: Solid Earth*, 118(10), 5442-5452, doi:10.1002/jgrb.50387.
- Heki, K. (2003), Snow load and seasonal variation of earthquake occurrence in Japan, *Earth and Planetary Science Letters*, 207(1), 159-164, doi:10.1016/S0012-821X(02)01148-2.
- Ide, S. (2010), Striations, duration, migration and tidal response in deep tremor, *Nature*, 466(7304), 356-359, doi:10.1038/nature09251.
- Ivins, E. R., T. S. James, and V. Klemann (2003), Glacial isostatic stress shadowing by the Antarctic ice sheet, *J. Geophys. Res.*, 108(B12), doi:10.1029/2002JB002182.

- Kilston, S., and L. Knopoff (1983), Lunar-solar periodicities of large earthquakes in southern California, *Nature*, *304*(5921), 21-25.
- Lowry, A. R. (2006), Resonant slow fault slip in subduction zones forced by climatic load stress, *Nature*, *442*(7104), 802-805, doi:10.1038/nature05055.
- Luttrell, K., and D. Sandwell (2010), Ocean loading effects on stress at near shore plate boundary fault systems, *Journal of Geophysical Research*, *115*(B8), doi:10.1029/2009jb006541.
- Lyard, F., F. Lefevre, T. Letellier, and O. Francis (2006), Modelling the global ocean tides: modern insights from FES2004, *Ocean Dynamics*, *56*(5), 394-415, doi:10.1007/s10236-006-0086-x.
- Namias, J. (1989), Summer earthquakes in southern California related to pressure patterns at sea level and aloft, *Journal of Geophysical Research: Solid Earth*, *94*(B12), 17671-17679, doi:10.1029/JB094iB12p17671.
- Ogata, Y. (1992), Detection of precursory relative quiescence before great earthquakes through a statistical model, *Journal of Geophysical Research*, *97*(B13), 19845, doi:10.1029/92jb00708.
- Pollitz, F. F. (1996), Coseismic deformation from earthquake faulting on a spherical earth, *Geophysical Journal International*, *125*, 1-14.
- Pollitz, F. F., A. Wech, H. Kao, and R. Bürgmann (2013a), Annual modulation of non-volcanic tremor in northern Cascadia, *Journal of Geophysical Research: Solid Earth*, *118*(5), 2445-2459, doi:10.1002/jgrb.50181.
- Pollitz, F. F., A. G. Wech, H. Kao, and R. Bürgmann (2013b), Annual modulation of non-volcanic tremor in northern Cascadia, *J. Geophys. Res.*, *118*, doi:10.1002/jgrb.50181.
- Reasenber, P. (1985), Second-order moment of central California seismicity, 1969–1982, *Journal of Geophysical Research*, *90*(B7), 5479, doi:10.1029/JB090iB07p05479.
- Reid, H. F. (1910), Permanent displacements of the ground, in the California earthquake of April 18, 1906, in *Report of the State Earthquake Investigation Commission*, edited, pp. 16-28, Carnegie Institution of Washington, Washington, D.C.
- Schuster, A. (1897), On lunar and solar periodicities of earthquakes, *Proc. R. Soc. Lond.*, *61*, 455-465.
- Shen, Z.-K., Q. Wang, R. Bürgmann, Y. Wan, and J. Ning (2005), Pole-Tide Modulation of Slow Slip Events at Circum-Pacific Subduction Zones, *Bulletin of the Seismological Society of America*, *95*(5), 2009-2015, doi:10.1785/0120050020.
- Tanaka, S. (2012), Tidal triggering of earthquakes prior to the 2011 Tohoku-Oki earthquake (Mw 9.1), *Geophysical Research Letters*, *39*(7), L00G26, doi:10.1029/2012GL051179.
- Tanaka, Y. (2014), An approximately 9-yr-period variation in seismicity and crustal deformation near the Japan Trench and a consideration of its origin, *Geophysical Journal International*, *196*(2), 760-787.
- Thomas, A. M., R. Bürgmann, D. R. Shelly, N. M. Beeler, and M. L. Rudolph (2012), Tidal triggering of low frequency earthquakes near Parkfield, CA: Implications for fault mechanics within the brittle-ductile transition, *J. Geophys. Res.*, *117*(B05301), doi:10.1029/2011JB009036.

- Tsai, V. C. (2011), A model for seasonal changes in GPS positions and seismic wave speeds due to thermoelastic and hydrologic variations, *Journal of Geophysical Research: Solid Earth*, 116(B4), doi:10.1029/2010JB008156.
- van Dam, T. (2010), NCEP Derived 6 hourly, global surface displacements at 2.5×2.5 degree spacing, [Available at <http://geophy.uni.lu/ncep-loading.html>.].
- Van Dam, T. M., and J. M. Wahr (1987), Displacements of the Earth's surface due to atmospheric loading: Effects on gravity and baseline measurements, *Journal of Geophysical Research: Solid Earth*, 92(B2), 1281-1286, doi:10.1029/JB092iB02p01281.
- van Stiphout, T., J. Zhuang, and D. Marsan (2012), Seismicity declustering, *Community Online Resource for Statistical Seismicity Analysis*, Available at <http://www.corssa.org>, doi:10.5078/corssa-52382934.
- Vidale, J. E., D. C. Agnew, M. J. S. Johnston, and D. H. Oppenheimer (1998), Absence of earthquake correlation with Earth tides: An indication of high preseismic fault stress rate, *J. Geophys. Res.*, 103, 24567-24572.
- Wahr, J. M. (1985), Deformation induced by polar motion, *Journal of Geophysical Research: Solid Earth*, 90(B11), 9363-9368, doi:10.1029/JB090iB11p09363.
- Wiemer, S., and M. Wyss (2000), Minimum Magnitude of Completeness in Earthquake Catalogs: Examples from Alaska, the Western United States, and Japan, *Bull. Seismol. Soc. Am.*, 90(4), 859-869.
- Zhuang, J., Y. Ogata, and D. Vere-Jones (2002), Stochastic Declustering of Space-Time Earthquake Occurrences, *Journal of the American Statistical Association*, 97(458), 369-380, doi:10.1198/016214502760046925.
- Zumberge, J. F., M. B. Heflin, D. C. Jefferson, M. M. Watkins, and F. H. Webb (1997), Precise point positioning for the efficient and robust analysis of GPS data from large networks, *Journal of Geophysical Research: Solid Earth*, 102(B3), 5005-5017, doi:10.1029/96JB03860.